Mechanism and Machine Theory 169 (2022) 104650

Contents lists available at ScienceDirect

Mechanism and Machine Theory

journal homepage: www.elsevier.com/locate/mechmt

Design of Single Degree-of-Freedom Triangular Resch Patterns with Thick-panel Origami

Fufu Yang [a,b], Miao Zhang [b,c], Jiayao Ma [b,c], Zhong You [d], Ying Yu [e], Yan Chen [b,c,*], Glaucio H. Paulino [f,g,h,*]

[a] School of Mechanical Engineering and Automation, Fuzhou University, Fuzhou 350116, China
[b] Key Laboratory of Mechanism Theory and Equipment Design of Ministry of Education, Tianjin University, Tianjin 300072, China
[c] School of Mechanical Engineering, Tianjin University, Tianjin 300072, China
[d] Department of Engineering Science, University of Oxford, Oxford OX1 3PJ, U.K.
[e] Department of Civil Engineering, Shantou University, Shantou 515063, China
[f] School of Civil and Environmental Engineering, Georgia Institute of Technology, Atlanta, GA 30332, USA
[g] Department of Civil and Environmnental Engineering, Princeton University, Princeton, New Jerseey 08544, USA
[h] Princeton Institute for the Science and Technology of Materials (PRISM), Princeton University, Princeton, New Jersey 08544, USA

ARTICLE INFO

Keywords:
Triangular Resch patterns
thick-panel origami
threefold-symmetric Bricard linkage
plane-symmetric Bricard linkage

ABSTRACT

As a series of tessellation origami patterns consisting of more than one type of polygons, Resch patterns are generally rigid foldable but with a large number of degrees of freedom (DOFs). The patterns are not flat foldable, instead the fully folded configuration is a sandwich style in flat profile. In order to achieve one-DOF forms of triangular Resch pattern units, the thick-panel technique is employed at vertices to replace spherical linkages with spatial linkages. The compatibility among all the vertices is studied by a systematic kinematic analysis of the thick-panel Resch pattern. Finally, two design schemes are obtained to form a one-DOF origami structure between the initial planar structure and the fully folded 3D sandwich structure with dome-curved intermediate folded configurations. The one-DOF Resch pattern structure can be used to generate reliable shape transformation.

1. Introduction

Ronald Dale Resch, a famous artist, computer scientist, and applied geometrist, discovered a family of origami tessellations in the 1960s by observing how paper crimps [1]. His first patent on tessellation structure [2] was invented after he had proposed three controlling restrictions, then the triangular Resch pattern in Fig. 1(a) was generated by decreasing the width of the "ribbon" while not altering the size or shape of the remainder of the structure [2, 3]. Similarly, there are some other tessellations constructed with regular planar tilings [4], see Fig. 1(b). Distinguished from other tessellations [5, 6], these structures can realize the transformation between the initial plate sheet and the final sandwich structure in flat profile through dome-like configurations [7], as shown in Fig. 1(c).

Constructed only with triangular pieces, the triangular Resch pattern in folded configuration presents higher stiffness with respect to other types of Resch's tessellations. Thus, it has application potential in engineering. Tachi presented an approach for the design of freeform variations of Resch-like origami tessellations from a given polyhedral surface [4]. Kshad et al. [8] fabricated Ron-Resch-like

* Corresponding author: Professor Yan Chen, Tianjin University, School of Mechanical Engineering, 92 Weijin Road, Tianjin, 300072, China
E-mail addresses: yan_chen@tju.edu.cn (Y. Chen), gp1863@princeton.edu (G.H. Paulino).

https://doi.org/10.1016/j.mechmachtheory.2021.104650
Received 4 February 2021; Received in revised form 25 October 2021; Accepted 8 November 2021
Available online 2 December 2021

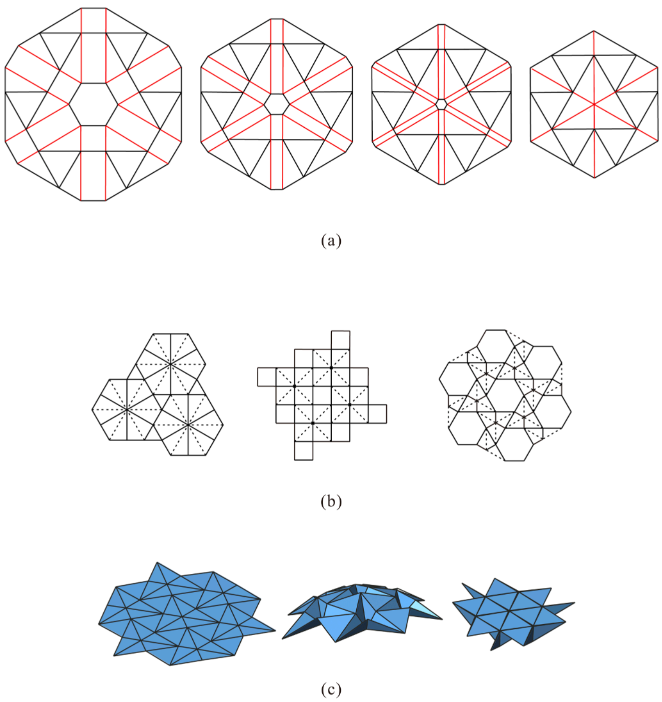

Fig. 1. Resch Patterns. (a)The evolution from Resch's first tessellation to the popular triangular Resch pattern [2]; (b) Other tessellations of the Resch patterns: triangular, quadrangular, and hexagonal pattern with the insertion of triangles [4]; (c) The folding of a triangular Resch pattern [7].

origami cores by 3D printing and tested those cores to show that they have advantages for damping impact forces and dissipating energy. A non-periodic Resch pattern was employed to construct a mechanical metamaterial and it was found that the structure displays an unusually strong load-bearing capability [9]. Magliozzi et al. [10] proposed two procedures for obtaining a folding/deploying path for the triangular Resch pattern, and they found that it is not possible to arbitrarily control all degrees of freedom of the pattern due to a halt in the folding/deployment path. Inspired by the triangular Resch pattern, Chen et al. [11] obtained a novel energy absorbing structure by 3D printing and selective laser sintering (SLS) - the elastic-plastic property of the Nylon material and the motion trend of the pattern were the main factors in the study. In civil engineering, Pesenti et al. [12] used shape memory alloys (SMA) as micro-actuators to drive the triangular Resch pattern to guarantee a relatively large displacement of the shading system for office buildings, such that the building could deliver visual comfort for users whilst reducing energy consumption for indoor climate control and artificial lighting. It was optimized and accessed by a thermal simulation method. Deng et al. [13] proposed and studied the performances of some foldcores based triangular-, quadrangular-, and hexagonal-Resch patterns.

However, these studies mainly focused on the mechanical performance of the Resch pattern and their kinematic folding process was not fully considered. Meanwhile, the operability of tessellated structures with a large number of multi-DOF units becomes more and more complicated. Numerical methods have been adopted to study the folding performance [1, 14], while no theoretical approach has been presented to precisely describe the folding process of such a multi-DOF origami. To make the Resch pattern suitable for wide applications with simple and controllable folding, it is necessary to find its variable forms with mobility as few as possible, ideally to be one. In rigid origami, there are two possible methods to reduce the system mobility while keeping the kinematic folding behaviours, vertex splitting [15, 16] and thick-panel transformation [17]. For the triangle Resch pattern, the vertex splitting is in fact the inverse process of Ronald Dale Resch in generating this pattern (Fig. 1(a)). On the other hand, the thick-panel transformation has yet to be applied to the Resch pattern, and our preliminary research shows that simply applying thick-panel transformation [17] to every vertex will lead to immobility of the whole pattern.

Therefore, in this paper, we will take the challenge to transform the zero-thickness Resch pattern into its thick-panel counterpart to produce a one-DOF thick-panel pattern by considering kinematic compatibility within a typical pattern unit. This paper is structured as follows. Section 2 analyses a unit of the triangular Resch pattern in thick-panel form by selecting spatial 6R linkages for its different vertices. Section 3 describes two constructing schemes of one-DOF thick-panel patterns with the combination of thick-panel and zero-thickness vertices and explores the design parameters to obtain feasible folding with no interference. Conclusions are drawn in Section 4.

2. Typical vertices of the Resch pattern and their thick-panel counterparts

The unit in the Resch pattern in Fig. 2(a) is threefold-symmetric and consists of two types of triangles, right- and equilateral- ones, such as triangles $A_1B_1C_1$ and $B_1C_1D_1$. From the view of crease pattern, vertex A_1 with six creases is of threefold-symmetry (Fig. 2(b)),

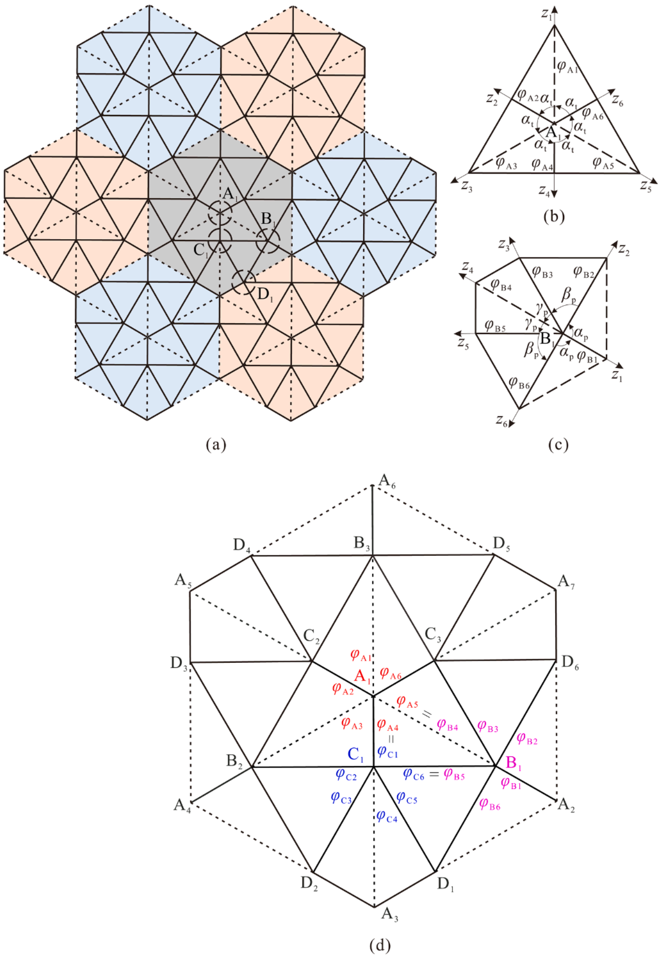

Fig. 2. Resch pattern. (a) General tessellation; (b) vertex A_1 and its surrounding creases; (c) vertex B_1 and its surrounding creases; (d) a typical unit of the Resch pattern.

and vertices B_1, C_1, and D_1 also with six creases are of plane symmetry (Fig. 2(c)).

All the vertices can be modeled as spherical 6*R* linkages. In general, one spherical 6*R* linkage has 3 DOFs. Therefore, the unit of the Resch pattern is a multi-DOF system [4, 18]. In order to get one-DOF forms of this unit, we employ the thick-panel transformation technique to replace some of the spherical 6*R* linkages with spatial 6*R* linkages that have one DOF by changing the zero-thickness panels into thick ones. As shown in Fig. 2(d), the pattern unit is geometrically in threefold-symmetry, hence the spherical 6*R* linkage at central vertex A_1 can be replaced with a threefold-symmetric Bricard linkage to obtain one DOF, in which three alternative creases z_1, z_3, and z_5 are set at the top sides of the panels with thickness l_A and the other three are set at the bottom ones as shown in Fig. 3(a). Namely, z_1, z_3, and z_5 intersected at one common point, so do z_2, z_4, and z_6, and these six creases exhibit threefold-symmetric property.

Its geometric conditions are [19]:

$$a_{12} = a_{23} = a_{34} = a_{45} = a_{56} = a_{61} = l_{\mathrm{A}}, \tag{1a}$$

$$\alpha_{12} = \alpha_{34} = \alpha_{56} = \alpha_{\mathrm{t}}, \quad \alpha_{23} = \alpha_{45} = \alpha_{61} = 2\pi - \alpha_{\mathrm{t}}, \tag{1b}$$

$$R_i = 0 \ \ (i = 1, 2, ..., 6), \tag{1c}$$

where $\alpha_{i(i+1)}$ is the twist angle and $a_{i(i+1)}$ is the link length of link $i(i+1)$, R_i is the offset of joint i, and $\theta_{\mathrm{A}i}$ is the revolute variable of joint i [20], $\alpha_{\mathrm{t}} = \pi/3$ (determined by Resch pattern). According to ref. [19], the kinematic equations are

$$\theta_{\mathrm{A1}} = \theta_{\mathrm{A3}} = \theta_{\mathrm{A5}}, \quad \theta_{\mathrm{A2}} = \theta_{\mathrm{A4}} = \theta_{\mathrm{A6}}, \tag{2a}$$

$$1 + 3(\mathrm{C}\theta_{\mathrm{A1}} + \mathrm{C}\theta_{\mathrm{A2}}) + 5\mathrm{C}\theta_{\mathrm{A1}}\mathrm{C}\theta_{\mathrm{A2}} - 4\mathrm{S}\theta_{\mathrm{A1}}\mathrm{S}\theta_{\mathrm{A2}} = 0, \tag{2b}$$

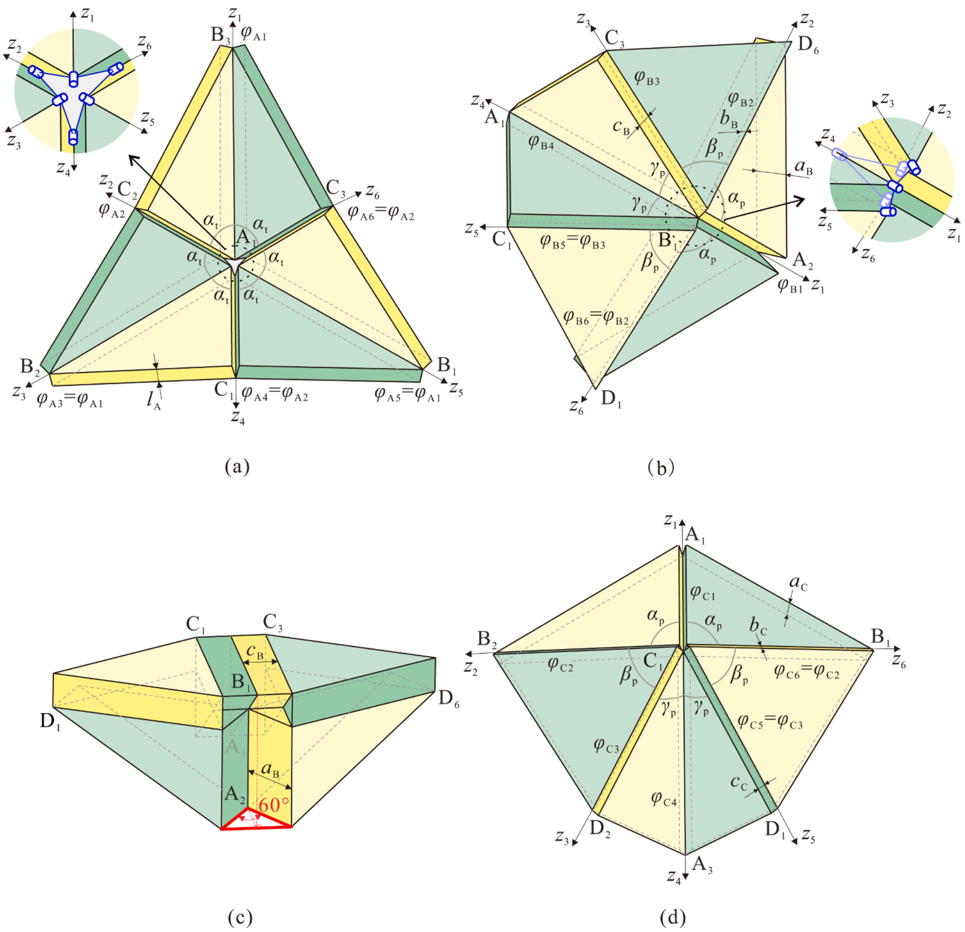

Fig. 3. Thick-panels. (a) The threefold-symmetric Bricard linkage at vertex A_1, (B) the plane-symmetric Bricard linkage at vertex B_1 and (c) its folded configuration, (d) the plane-symmetric Bricard linkage at vertex C_1.

in which C and S indicate cosine and sine, respectively. Here, thickness l_A does not affect kinematics.

To illustrate its kinematics more intuitively, dihedral angles between adjacent panels, $\varphi_{Ai}(i = 1, 2, 3, 4, 5, 6)$, are adopted. Then in vertex A_1

$$\varphi_{Ai} = \begin{cases} \pi + \theta_{Ai}, (i = 1, 3, 5) \\ \pi - \theta_{Ai}, (i = 2, 4, 6) \end{cases}. \tag{3}$$

Thus, its kinematic relations, provided by Eqs. (2), become

$$\varphi_{A1} = \varphi_{A3} = \varphi_{A5}, \quad \varphi_{A2} = \varphi_{A4} = \varphi_{A6}, \tag{4a}$$

$$\tan(\varphi_{A2} / 2) = 2\tan(\varphi_{A1} / 2) + \sqrt{3(\tan^2(\varphi_{A1}/2) + 1)}. \tag{4b}$$

For B_k (k=1, 2, 3), see Figs. 2(c) and 3(b), the spherical 6*R* linkages can be replaced with plane-symmetric Bricard 6*R* linkages [21], see the right insert in Fig. 3(b). The *R*-joints are marked by the axes z_i and three kinds of panels with thickness *a, b, c* are used. Here, these six axes exhibit the property of being plane-symmetric. The kinematic derivation of the spherical 6*R* and the plane-symmetric Bricard linkages can be found in Appendices A and B, respectively.

The geometrical conditions of the plane-symmetric Bricard linkage are

$$a_{12} = a_{61} = a, \quad a_{23} = a_{56} = b, \quad a_{34} = a_{45} = c, \tag{5a}$$

$$\alpha_{12} = -\alpha_{61} = \alpha_p, \quad \alpha_{23} = -\alpha_{56} = \beta_p, \quad \alpha_{34} = -\alpha_{45} = \gamma_p, \tag{5b}$$

$$R_1 = R_4 = 0, \quad R_2 = -R_6 = r_2, \quad R_3 = -R_5 = r_3, \tag{5c}$$

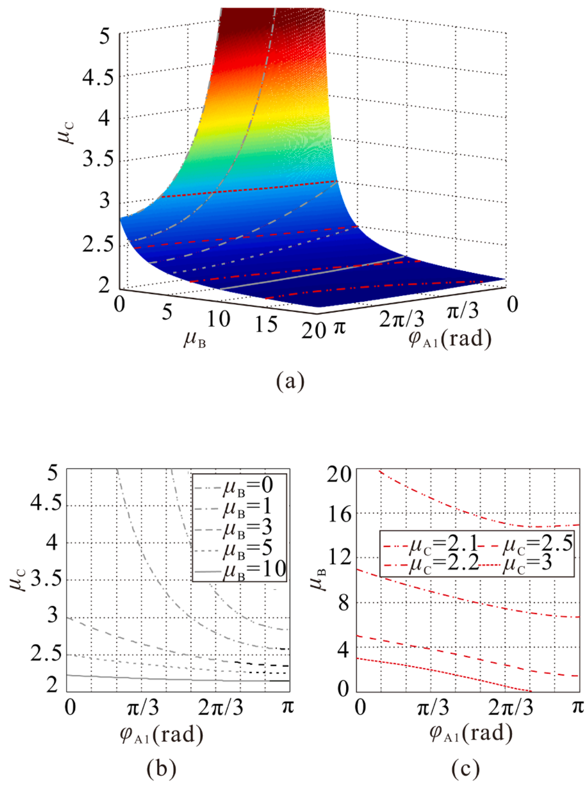

Fig. 4. The relationship among φ_{A1}, μ_B and μ_C to show the geometric incompatibility when vertices A_1, B_1, and C_1 are all set spatial linkages at the same time. (a) μ_C versus φ_{A1} and μ_B; (b) μ_C versus φ_{A1} for $\mu_B=0$, $\mu_B=1$, $\mu_B=3$, $\mu_B=5$, $\mu_B=10$; (c) μ_B versus φ_{A1} for $\mu_C=2.1$, $\mu_C=2.2$, $\mu_C=2.5$, $\mu_C=3$.

in which, α_p, β_p, γ_p, r_2, and r_3 are determined by the Resch pattern,

$$\alpha_p=\pi/2,\quad \beta_p=\pi/3,\quad \gamma_p=\pi/6. \tag{6a}$$

$$r_2=r_3=0\,. \tag{6b}$$

Substituting geometric conditions, Eqs. (6), into the kinematic equations of the general plane-symmetric Bricard linkage [21], we obtain the kinematic equations as Eqs. (B2).

Similarly to vertex A_1, the dihedral angles of adjacent panels, $\varphi_i(i=1,2,3,4,5,6)$, are adopted as

$$\varphi_1=\theta_1,\quad \varphi_4=-\theta_4,\quad \varphi_i=\pi+\theta_i\ \ (i=2,3,5,6), \tag{7a}$$

$$\varphi_6=\varphi_2,\quad \varphi_5=\varphi_3. \tag{7b}$$

The relationship among dihedral angles is derived in Appendix B and presented as Eq. (B4).

Since the thick-panel unit is the combination of the one-DOF 6*R* linkages and the original spherical 6*R* linkages, it is essential to distinguish vertices B_k and C_k. Therefore, subscripts B and C for *a, b, c* as well as $\theta_i(i=1,\ 2,\ \ldots,\ 6)$ will be adopted to distinguish them.

Meanwhile, to completely fold the linkage, as shown in Fig. 3(c), the top surfaces of panels $A_1B_1C_1$ and $A_1B_1C_3$ coincide and these panels fulfill the gap between panels $B_1C_1D_1$ and $B_1C_3D_6$ with thickness $2c_B$. Moreover, the thickness of panels $B_1A_2D_1$, $B_1A_2D_6$, being both a_B, and that of panel $A_1B_1C_1$- $A_1B_1C_3$ form a right triangle which is marked with thick lines in Fig. 3(c). Thus,

$$a_B=2c_B. \tag{8a}$$

Similarly,

$$a_C=2c_C. \tag{8b}$$

By replacing the spherical 6*R* linkages with Bricard linkages, we have essentially added constraints to each vertex. In what follows, we will investigate the compatibility among these vertices to make sure the unit will be mobile and then design panel thicknesses to physically realize the constraints such that we achieve a one-DOF unit of the Resch pattern.

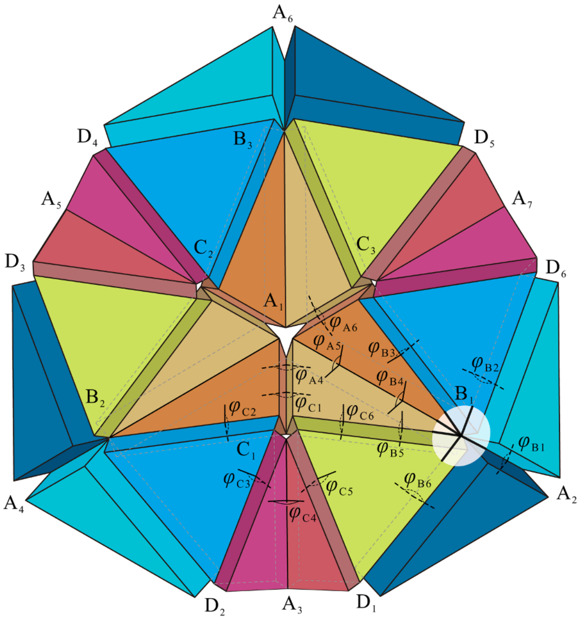

(a)

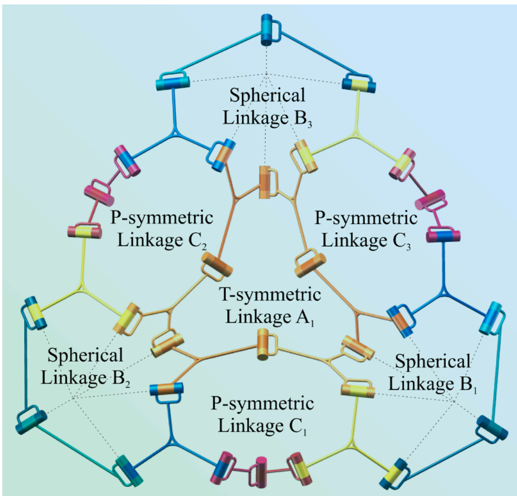

(b)

Fig. 5. Constructing of scheme I, (a) the thick-panel origami, and (b) its mechanism.

3. One-dof thick-panel origami of the Resch unit

In this section, we provide the theoretical construction to achieve one-DOF thick Resch pattern units. First, the kinematics and compatibility relations using spatial linkages are addressed, and then two alternative schemes are provided.

3.1. Compatibility of loop A_1-B_1-C_1 with three spatial linkages

For the unit in Fig. 2(d), the motion at vertices B_1, B_2, B_3 are identical with respect to A_1, so are vertices C_1, C_2, C_3 due to the threefold symmetry of the unit. Hence, the kinematic loop A_1-B_1-C_1 in the thick-panel form will be studied in detail.

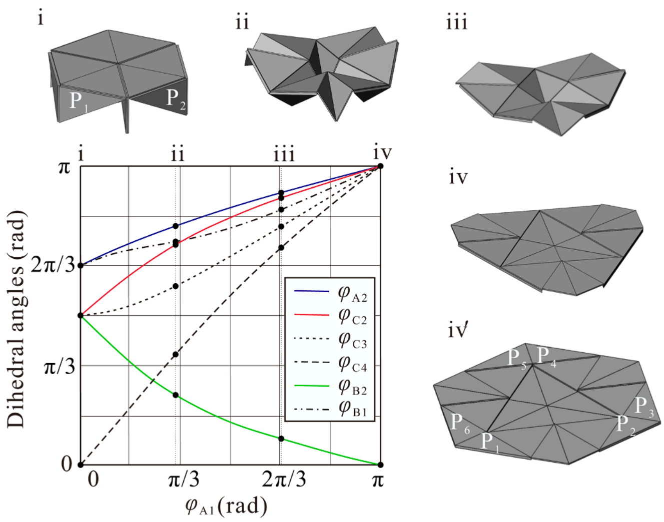

Fig. 6. The relationships between the dihedral angles and the input variable of scheme I with $\mu_C = 1$.

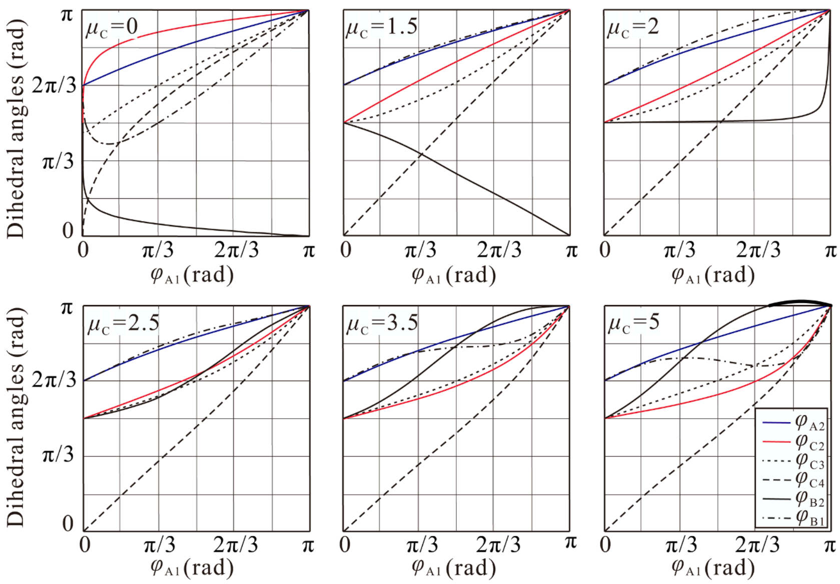

Fig. 7. The kinematic relationships of scheme I with varying μ_C.

If we directly convert all of the spherical 6*R* linkages at vertices A_1, B_1, C_1 to overconstrained spatial 6*R* linkages to obtain the thick-panel form, $l_A \neq 0$, ${a_B}^2 + {b_B}^2 + {c_B}^2 \neq 0$, and ${a_C}^2 + {b_C}^2 + {c_C}^2 \neq 0$. The relationships among the design parameters of these overconstrained linkages to obtain a movable loop with one DOF are studied next.

For vertex B_1, if $c_B = 0$, then $a_B = 0$ according to Eq. (8a), and Eq. (B1c) becomes

$$(1 + C\varphi_{B1}) \cdot b_B \cdot C\varphi_{B2} = 0. \tag{9}$$

Notice that φ_{B1} and φ_{B2} are kinematic variables, so $b_B = 0$ makes Eq. (9) stand, which results in the fact that the vertex B turns back to the spherical 6*R* linkage again. Therefore, $c_B \neq 0$ must be satisfied. Moreover, $\mu_B = b_B / c_B$ is defined as a design variable of the linkage.

Similarly to vertex B_1, at vertex C_1, $c_C \neq 0$. $\mu_C = b_C / c_C$ is also defined as a design variable of the linkage.

As these three linkages are connected to each other forming the loop A_1-B_1-C_1, there are relationships among their kinematic variables. As shown in Fig. 2(d), the linkages at vertices A_1 and B_1 share two adjacent panels, which results in the equivalence of corresponding dihedral angles,

$$\varphi_{B4} = \varphi_{A5} (= \varphi_{A1}). \tag{10a}$$

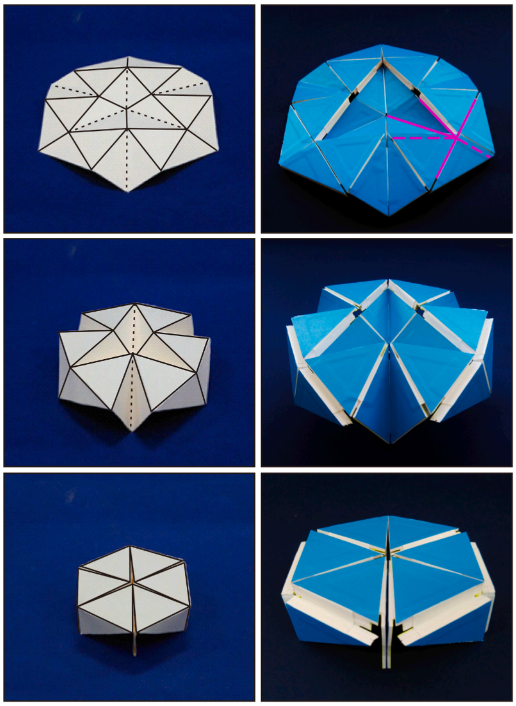

Fig. 8. Folding sequence of the physical model of scheme I for the thick Resch pattern with $\mu_C = 3$, and six revolute axes of a spherical 6*R* linkage are marked in the picture on the top right, where dashed lines are for invisible lines.

The linkage at C_1 is connected with both linkages at A_1 and B_1, so the compatible conditions are,

$$\varphi_{C1} = \varphi_{A4}(= \varphi_{A2}), \tag{10b}$$

$$\varphi_{C6}(= \varphi_{C2}) = \varphi_{B5}(= \varphi_{B3}). \tag{10c}$$

Combining Eqs. (10a), (B4a), (10c), (B5a), (B4c), (10b), and (4b), the relationship among the input variable φ_{A1}, design variables μ_B and μ_C can be obtained.

In order to make the assembly rigid-foldable, the relationship must be tenable for any φ_{A1}, while μ_B and μ_C are constant design parameters. However, as shown in Fig. 4, μ_B and μ_C vary with φ_{A1} along the folding path, so the structure is immobile when vertices A_1, B_1, and C_1 are replaced with spatial linkages at the same time. To make it mobile, some constraints have to be released, namely keeping some vertices as spherical 6*R* linkages.

Since the kinematics of threefold-symmetric spherical 6*R* linkage and threefold-symmetric Bricard linkage are identical, to set vertex A_1 as a spherical 6*R* linkage while keeping the threefold symmetry and replace vertices B_1 and C_1 with plane-symmetric Bricard 6*R* linkage, the relationship among all the kinematic variables are the same as the case the vertex A_1 is set a threefold-symmetric Bricard linkage. Hence the zero-thickness vertex A_1 and thick-panel vertices B_1 and C_1 will also generate an immobile unit.

Therefore, there are two possible schemes, **(I)** vertex B_1 is kept as a spherical 6*R* linkage, $a_B = b_B = c_B = 0$, and vertices A_1 and C_1 are in the thick-panel forms; **(II)** vertex C_1 is a spherical 6*R* linkage, $a_C = b_C = c_C = 0$, and vertices A_1 and B_1 are in the thick-panel forms.

3.2. Construction of scheme I for thick Resch panel

In scheme I, vertex B_1 is set as a spherical 6*R* linkage - see six white panels around vertex B_1 in Fig. 5, while vertices A_1 and C_1 are still kept as threefold-symmetric (T-symmetric) and plane-symmetric (P-symmetric) Bricard linkages, respectively. Hence, the thick-panel origami structure is constructed with a threefold-symmetric Bricard linkage A_1, three identical plane-symmetric Bricard linkages C_1, C_2, C_3, and three identical spherical 6*R* linkages B_1, B_2, B_3. Linkages A_1 and C_i have one DOF, while linkage B_i has three DOFs. For the linkage loop A_1-B_1-C_1, $\varphi_{A4} = \varphi_{C1}$ can drive linkages A_1 and C_1 at the same time. And in the loop A_1-B_1-C_3, C_3 and C_1 move in the same manner, $\varphi_{A6} = \varphi_{C1}$ with $\varphi_{A6} = \varphi_{A4}$ due to symmetry. Subsequently, the outputs of linkages A_1, C_1 and C_3 on creases A_1B_1, C_1B_1, C_3B_1 drive linkage B_1 simultaneously to guarantee the default motion on other creases because the spherical 6*R* linkage is normally with 3 DOFs. Since all kinematic variables can be expressed only by one input, φ_{A1}, there is only one independent variable to define the configuration, thus the whole linkage is with one DOF [22]. The detailed relationship among kinematic variables is derived in Appendices A and B, which has also been verified by the truss-transformation method [23, 24]. A brief introduction of the truss-transformation method is given in Appendix C.

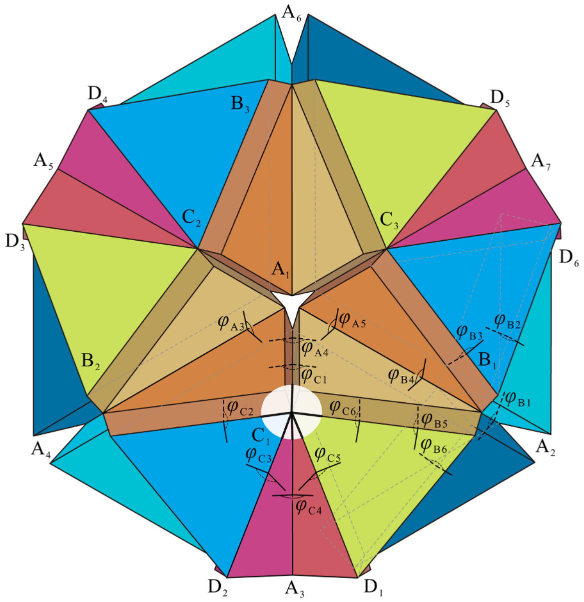

(a)

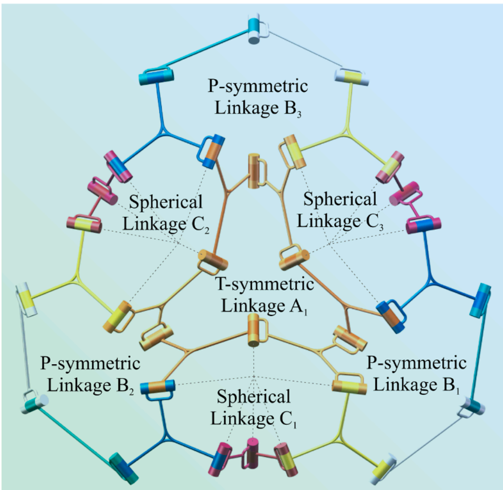

(b)

Fig. 9. Constructing of scheme II, (a) the thick-panel origami, and (b) its mechanism.

The panel thickness will affect the structure motion. In this construction scheme, linkage A_1 is a threefold-symmetric Bricard linkage, whose kinematics is not related to the link length (panel thickness), linkages B_i are in the zero-thickness form, and the thickness of linkages C_i are set as in the last section. So $\mu_C = b_C/c_C$ is the design variable for the kinematics of this thick-panel structure. Here, $\mu_C = 1$ is chosen at first, and other values will be studied in detail later. Figure 6 represents the relationships of the input variable and the other dihedral angles in the folding process.

When the dihedral angle $\varphi_{A1} = 0$, φ_{C4} goes to 0, both φ_{A2} and φ_{B1} reach $2\pi/3$, while φ_{C2}, φ_{C3}, and φ_{B2} reach $\pi/2$. Thus, the thick-panel origami can reach the folded configuration, see configuration i in Fig. 6. However, at the deployed configuration, namely $\varphi_{A1} = \pi$, the dihedral angle φ_{B2} becomes zero, and it means that the outer panels P_1-P_6 are folded towards the center of the structure (see configuration iv in Fig. 6), rather than flattened, i.e., $\varphi_{B2} = \pi$ (see the desired configuration iv' in Fig. 6). Due to the difference of thickness of panels, the underside of the structure is not in a plane (see Fig. 5), and $\varphi_{B2} = 0$ must render physical interference between the outer- and the center panels.

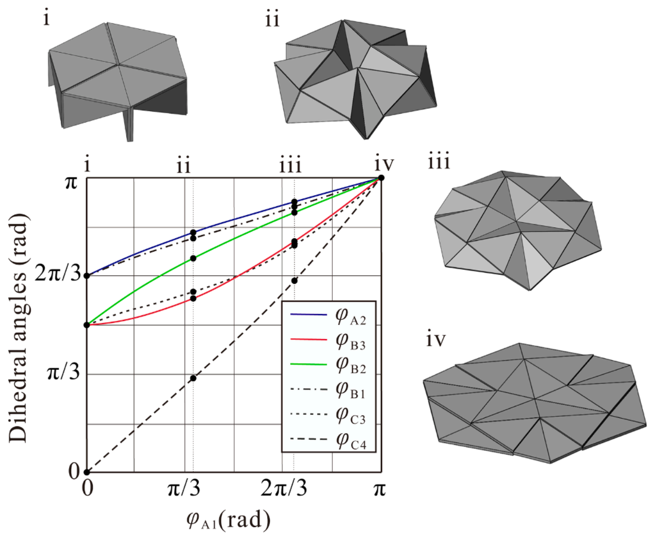

Fig. 10. The relationships between the dihedral angles and the input variable of scheme II with $\mu_B = 1$.

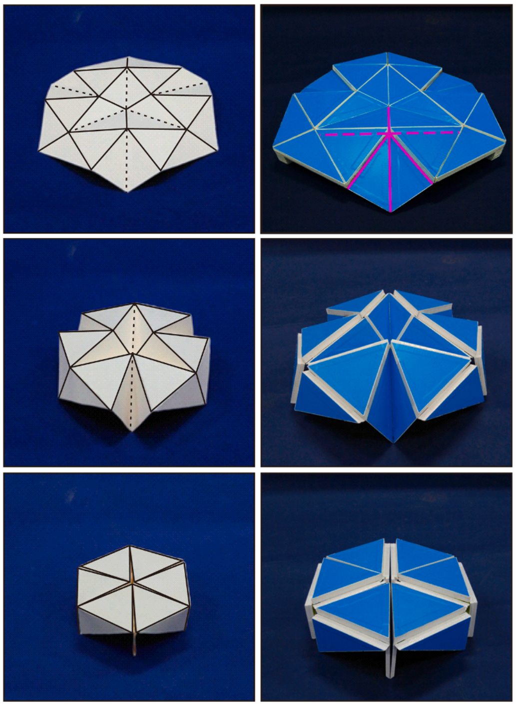

Fig. 11. Folding sequence of the physical model of scheme II for the thick Resch pattern with $\mu_B = 1$, and six revolute axes of a spherical 6*R* linkage are marked in the picture on the top right, where dashed lines are for invisible lines.

Figure 7 shows the kinematic curves of dihedral angles with different μ_C. When $0 \leq \mu_C < 2.0$, the dihedral angle φ_{B2} varies from $\pi/2$ to 0 instead of π during the deployment from the folded configuration to the planar configuration, implying the existence of physical interference. When $\mu_C > 3.5$, φ_{B2} exceeds π before reaching the planar configuration, see the right section of the top curve in the last diagram in Fig. 7, which results in interference before the completely deployed configuration. When $2.0 \leq \mu_C \leq 3.5$, the structure could fold steadily without interference. The range of μ_C is found by the parameter sweep technique. Therefore, the design variable μ_C of scheme I should be chosen within this range to avoid interference of panels and to get the expected motion of folding.

It should be noticed that the relationship between link lengths c_B and l_A does not affect the mobility of the whole structure, however, their values are always chosen to be equal to avoid uneven surface at deployed configuration. A one-DOF thick-panel origami was manufactured and shows good agreement with its zero-thickness counterpart in terms of folding sequence when $\mu_C = 3$, with

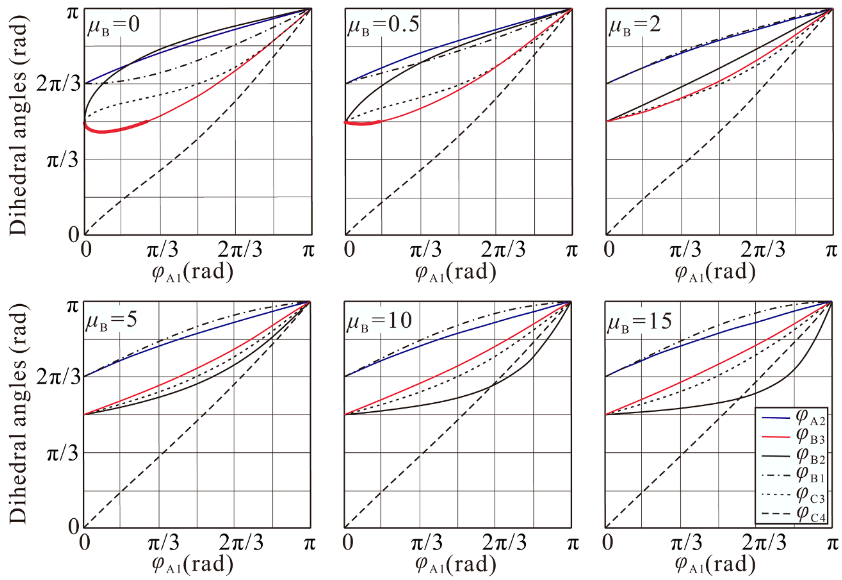

Fig. 12. The kinematic relationships of scheme II with varying μ_B.

design thicknesses $l_A = 20$mm, $a_C = l_A = 20$mm, $c_C = a_C/2 = 10$mm, and $b_C = \mu_C \cdot c_C = 30$mm, as shown in Fig. 8, and thus the prototype folds with no interference.

3.3. Construction of scheme II

In scheme II, vertex C_1 is set as a spherical 6*R* linkage - see six white panels around C_1 in Fig. 9, while vertices A_1 and B_1 are kept as threefold-symmetric and plane-symmetric Bricard linkages, respectively. Linkages A_1 and B_i have one DOF, while linkage C_i has three DOFs. For the linkage loop A_1-B_1-C_1, $\varphi_{A5} = \varphi_{B4}$ can drive linkages A_1 and B_1 at the same time. In the loop A_1-B_2-C_1, B_2 and B_1 move in the same manner, and $\varphi_{A3} = \varphi_{B4}$ with $\varphi_{A3} = \varphi_{A5}$ due to symmetry. Then the outputs of linkages A_1, B_1 and B_2 on creases A_1C_1, B_1C_1, B_2C_1 drive linkage C_1 simultaneously to guarantee the default motion on other creases. Therefore, there is only one independent variable to define the configuration, and the structure has one DOF [22], which has been verified by the truss-transformation method [23, 24]. The detailed relationship among kinematic variables is derived in Appendices A and B to assess whether the thick-panel origami could realize the deployment between the planar and the folded sandwich configurations.

Similarly to the previous scheme, $\mu_B = b_B/c_B$ is the design parameter for the kinematics of this thick-panel unit. Here, μ_B is also set to one at first. Figure 10 shows that the structure could realize the transformation between the folded configuration (configuration i in Fig. 10), $\varphi_{A1} = \varphi_{B4} = \varphi_{C4} = 0$, $\varphi_{A2} = \varphi_{B1} = \varphi_{C1} = 2\pi/3$, $\varphi_{B2} = \varphi_{B3} = \varphi_{C2} = \varphi_{C3} = \pi/2$, and the planar configuration (configuration iv in Fig. 10), $\varphi_{C1} = \varphi_{C2} = \varphi_{C3} = \varphi_{C4} = \pi$, $\varphi_{B1} = \varphi_{B2} = \varphi_{B3} = \varphi_{B4} = \pi$, $\varphi_{A1} = \varphi_{A2} = \pi$.

Figure 11 shows a physical model of scheme II when $\mu_B = 1$, which folds with no interference. Its design thicknesses are $l_A = 10$mm, $c_B = l_A = 10$mm, $a_B = 2c_B = 20$mm, and $b_B = \mu_B \cdot c_B = 10$mm.

The kinematic curves of dihedral angles are plotted with different μ_B, as shown in Fig. 12. When $0 \le \mu_B \le 0.99$, there are some configurations with $\varphi_{B3} < \pi/2$ before the fully folded configuration, which results in physical interference, such as the thick red curve in the first two graphs of Fig. 12. When $\mu_B > 0.99$, with an increase in μ_B, φ_{B3} tends to undergo a smooth change at first and then a rapid change afterward, while the other dihedral angles vary smoothly throughout the entire folding sequence. The results illustrate that μ_B of scheme II should be larger than 0.99 in order to avoid physical interference. The range of μ_B is also determined by the parameter sweep technique.

4. Concluding remarks

In this paper, a unit of Resch pattern, which is a multi-DOF and zero-thickness origami tessellation, is studied and two thick-panel counterparts with one DOF are designed. According to the thick-panel transformation, each vertex is replaced with a corresponding spatial linkage. Compatibility analysis shows that the replacement can not be conducted for all the vertices at the same time. Two schemes of constructing a one-DOF thick-panel origami by releasing some constraints are developed and analyzed with kinematic compatibility. Parametric studies show that both of them can realize the deployment between planar and fully-folded configurations with one DOF via dome-curved intermediate folding configurations when proper design parameters are adopted. One physical prototype of each feasible scheme was manufactured to validate the analysis method.

To extend the application of the Resch pattern, units are always expected to be tessellated to larger structures. However, tessellating these units directly will get immovable structures due to existence of overconstraint. Thus, some particular constraints should be released to make the structure movable and with lower mobility, which is a topic for future investigation. Furthermore, since the zero-thickness Resch pattern has multi-DOFs, it can realize a variety of curved surfaces more flexibly than that constructed with the Miura-ori [25]. Therefore, adopting a Resch pattern to realize some particular surfaces with fewer DOFs is another formidable challenge.

Declaration of Competing Interest

The authors declare no conflict of interest

Acknowledgments

YC would like to thank the financial support from the National Natural Science Foundation of China (Project Nos. 51825503, 52035008 and 51721003). FY thanks to the support from the National Natural Science Foundation of China (Project No. 51905101) and the Natural Science Foundation of Fujian Province, China (Project No. 2019J01209). The authors gratefully thank Mrs. Emily D. Sanders for helpful comments which contributed to improving this manuscript.

APPENDIX A. Kinematics of plane-symmetric spherical 6*R* linkages

This appendix shows the kinematics of plane-symmetric spherical 6*R* linkage, in which three kinematic variables are the input. The results are both suitable for the spherical linkage at B_1 for Scheme I, and the spherical linkage at C_1 for Scheme II in the text. It should be noticed that subscripts B and C should be added accordingly to kinematic variables θ and φ for these two linkages.

For spherical 6*R* linkages, the closure equation is

$$\mathbf{Q}_{12}\cdot\mathbf{Q}_{23}\cdot\mathbf{Q}_{34}=\mathbf{Q}_{16}\cdot\mathbf{Q}_{65}\cdot\mathbf{Q}_{54} \tag{A1}$$

where $\mathbf{Q}_{ij}$ represents the coordinate transformation between systems i and j. The plane-symmetric spherical 6*R* linkage for vertices B_k and C_k is shown in Fig. A1. The geometrical conditions are

$$\alpha=\pi/2,\quad \beta=\pi/3,\quad \gamma=\pi/6,\quad \varphi_2=\varphi_6,\quad \varphi_3=\varphi_5 \tag{A2}$$

where φ_i represents dihedral angles between adjacent facets. And the relationships between kinematic variables and dihedral angles are

$$\theta_1=\pi-\varphi_1,\quad \theta_2=\pi-\varphi_2,\quad \theta_3=\pi-\varphi_3,\quad \theta_4=\varphi_4-\pi \tag{A3}$$

By substituting Eqs. (A2-A3) into Eq. (A1), the entries (1, 3), (2, 3) and (3, 1) in Eq. (A1) are obtained as

$$2C\varphi_2S\varphi_3C\varphi_1+S\varphi_2C\varphi_3C\varphi_1+S\varphi_2C\varphi_3+2C\varphi_2S\varphi_3-3S\varphi_2C\varphi_1+\sqrt{3}C\varphi_3S\varphi_1-3S\varphi_2+\sqrt{3}S\varphi_1=0 \tag{A4}$$

$$2C\varphi_2S\varphi_3S\varphi_1+S\varphi_2C\varphi_3S\varphi_1-3S\varphi_2S\varphi_1-\sqrt{3}C\varphi_3C\varphi_1+\sqrt{3}C\varphi_3-\sqrt{3}S\varphi_1+\sqrt{3}=0 \tag{A5}$$

$$\begin{aligned}&2\sqrt{3}S\varphi_2S\varphi_3S\varphi_4-\sqrt{3}C\varphi_2C\varphi_3S\varphi_4+2C\varphi_2S\varphi_3C\varphi_4+4S\varphi_2C\varphi_3C\varphi_4+2C\varphi_2S\varphi_3+4S\varphi_2C\varphi_3\\&-\sqrt{3}C\varphi_2S\varphi_4=0\end{aligned} \tag{A6}$$

By simplifying entries (2, 3) and (3, 1), the Eq. (A5) and Eq. (A6) are rewritten as

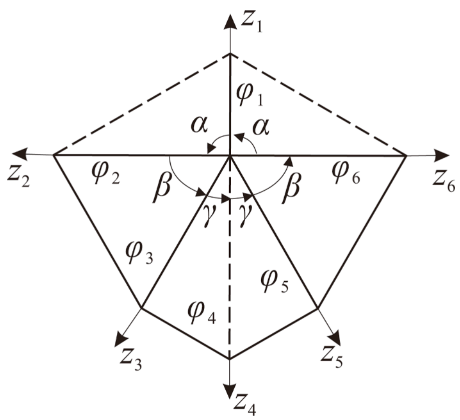

Fig. A1. A plane-symmetric spherical 6*R* linkage with kinematic parameters.

$$\tan(\varphi_1/2) = -\frac{\sqrt{3}}{3}\frac{S\varphi_2C\varphi_3 + 2C\varphi_2S\varphi_3 - 3S\varphi_2}{1 + C\varphi_3} \tag{A7}$$

$$\tan(\varphi_4/2) = \frac{4\sqrt{3}}{3}\frac{C\varphi_2S\varphi_3 + 2S\varphi_2C\varphi_3}{2C\varphi_2 - 4S\varphi_2S\varphi_3 + 2C\varphi_2C\varphi_3} \tag{A8}$$

With Eq. (A4), the kinematic relationship among φ_3, φ_1 andφ_2 is obtained as

$$(2C\varphi_2C\varphi_1 + 2C\varphi_2)S\varphi_3 + \left(S\varphi_2C\varphi_1 + S\varphi_2 + \sqrt{3}S\varphi_1\right)C\varphi_3 - \left(3S\varphi_2C\varphi_1 + 3S\varphi_2 - \sqrt{3}S\varphi_1\right) = 0. \tag{A9}$$

Then, $\varphi_3 = \varphi_5$ is explicitly expressed by φ_1 and φ_2 as

$$\tan(\varphi_3/2) = \frac{2U_1 + \sqrt{4U_1{}^2 + 4U_2{}^2 - 4U_3{}^2}}{2U_2 + 2U_3}, \tag{A10}$$

in which

$$U_1 = C\varphi_2C\varphi_1/2 + C\varphi_2/2,$$

$$U_2 = S\varphi_2C\varphi_1\Big/4 + S\varphi_2\Big/4 + \sqrt{3}S\varphi_1\Big/4,$$

$$U_3 = 3S\varphi_2C\varphi_1\Big/4 + 3S\varphi_2\Big/4 - \sqrt{3}S\varphi_1\Big/4.$$

With Eq. (A6), the kinematic relationship among φ_2, φ_3 and φ_4 is obtained as

$$\tan\varphi_2 = \frac{\sqrt{3}S\varphi_4(C\varphi_3 + 1) - 2S\varphi_3(C\varphi_4 + 1)}{2\sqrt{3}S\varphi_3S\varphi_4 + 4C\varphi_3C\varphi_4 + 4C\varphi_3}. \tag{A11}$$

APPENDIX B. Kinematics of P-symmetric Bricard 6*R* linkages

Since plane-symmetric Bricard 6*R* linkage has one DOF, it can move determinately with one driver, and all kinematic variables could be expressed by each other. This appendix shows the derivation of some expressions. The results are both suitable for the spatial linkage at C_1 for Scheme I, and the spatial linkage at B_1 for Scheme II in the text. It should be noticed that subscripts C and B should be added accordingly to design parameters *a, b, c*, μ and kinematic variables θ and φ for these two spatial linkages.

According to ref. [21], the kinematic equations of the general plane-symmetric Bricard linkages are

$$\theta_2 = \theta_6, \quad \theta_3 = \theta_5, \tag{B1a}$$

$$\begin{aligned} &S\theta_1\left(C\alpha_pS\gamma_pS\theta_2S\theta_3 - C\alpha_pC\beta_pS\gamma_pC\theta_2C\theta_3 + S\alpha_pS\beta_pS\gamma_pC\theta_3 - C\alpha_pS\beta_pC\gamma_pC\theta_2 - S\alpha_pC\beta_pC\gamma_p\right) \\ &= (1 + C\theta_1)\left(S\gamma_pC\theta_2S\theta_3 + C\beta_pS\gamma_pS\theta_2C\theta_3 + S\beta_pC\gamma_pS\theta_2\right) \end{aligned} \tag{B1b}$$

$$\begin{aligned} &S\theta_1\left[c\left(C\alpha_pS\theta_2C\theta_3 + C\alpha_pC\beta_pC\theta_2S\theta_3 - S\alpha_pS\beta_pS\theta_3\right) + bC\alpha_pS\theta_2 - R_3C\alpha_pS\beta_pC\theta_2 - R_2S\alpha_p \right. \\ &\left. -R_3S\alpha_pC\beta_p\right] = (1 + C\theta_1)\left[c\left(C\theta_2C\theta_3 - C\beta_pS\theta_2S\theta_3\right) + bC\theta_2 + a + R_3S\beta_pS\theta_2\right] \end{aligned} \tag{B1c}$$

$$\begin{aligned} &(1 + C\theta_4)\left(S\alpha_pS\theta_2C\theta_3 + S\alpha_pC\beta_pC\theta_2S\theta_3 + C\alpha_pS\beta_pS\theta_3\right) = S\theta_4\left[C\gamma_p(S\alpha_pS\theta_2S\theta_3 - S\alpha_pC\beta_pC\theta_2C\theta_3 \right. \\ &\left. -C\alpha_pS\beta_pC\theta_3) + S\gamma_p\left(S\alpha_pS\beta_pC\theta_2 - C\alpha_pC\beta_p\right)\right] \end{aligned}. \tag{B1d}$$

in which thicknesses *a, b*, and *c* are the design parameters. By considering geometric conditions, Eqs. (6a) and (6b), the above equations, Eq. (B1), can be simplified as

$$\theta_2 = \theta_6, \quad \theta_3 = \theta_5, \tag{B2a}$$

$$S\theta_1\left(\frac{\sqrt{3}}{4}C\theta_3 - \frac{\sqrt{3}}{4}\right) = (1 + C\theta_1)\left(\frac{1}{2}C\theta_2S\theta_3 + \frac{1}{4}S\theta_2C\theta_3 + \frac{3}{4}S\theta_2\right), \tag{B2b}$$

$$S\theta_1\left(-\frac{\sqrt{3}}{2}cS\theta_3\right) = (1 + C\theta_1)\left[c\left(C\theta_2C\theta_3 - \frac{1}{2}S\theta_2S\theta_3\right) + bC\theta_2 + a\right], \tag{B2c}$$

$$(1 + C\theta_4)\left(S\theta_2C\theta_3 + \frac{1}{2}C\theta_2S\theta_3\right) = \frac{\sqrt{3}}{4}S\theta_4(2S\theta_2S\theta_3 - C\theta_2C\theta_3 + C\theta_2). \tag{B2d}$$

Dihedral angles, Eq. (7), were used, and the above equations become

$$\varphi_2 = \varphi_6, \quad \varphi_3 = \varphi_5, \tag{B3a}$$

$$S\varphi_1\left(-\frac{\sqrt{3}}{4}C\varphi_3 - \frac{\sqrt{3}}{4}\right) = (1 + C\varphi_1)\left(\frac{1}{2}C\varphi_2 S\varphi_3 + \frac{1}{4}S\varphi_2 C\varphi_3 - \frac{3}{4}S\varphi_2\right), \tag{B3b}$$

$$S\varphi_1\left(\frac{\sqrt{3}}{2}cS\varphi_3\right) = (1 + C\varphi_1)\left[c\left(C\varphi_2 C\varphi_3 - \frac{1}{2}S\varphi_2 S\varphi_3\right) - bC\varphi_2 + a\right], \tag{B3c}$$

$$(1 + C\varphi_4)\left(S\varphi_2 C\varphi_3 + \frac{1}{2}C\varphi_2 S\varphi_3\right) = -\frac{\sqrt{3}}{4}S\varphi_4(2S\varphi_2 S\varphi_3 - C\varphi_2 C\varphi_3 - C\varphi_2). \tag{B3d}$$

According to Eqs. (B3b)- (B3d), the relationship between φ_4 and φ_2 are

$$S_1\tan^4(\varphi_2/2) + S_2\tan^3(\varphi_2/2) + S_3\tan^2(\varphi_2/2) + S_4\tan(\varphi_2/2) + S_5 = 0, \tag{B4a}$$

where

$$S_1 = -4bc - b^2 - 3c^2,$$

$$S_2 = 4\sqrt{3}bc\tan(\varphi_4/2) + 8\sqrt{3}c^2\tan(\varphi_4/2),$$

$$S_3 = 2b^2 + 6c^2,$$

$$S_4 = -4\sqrt{3}bc\tan(\varphi_4/2) + 8\sqrt{3}c^2\tan(\varphi_4/2).$$

According to Eqs. (B3b) and (B3c), the relationship between φ_3 and φ_2 are

$$\tan(\varphi_3/2) = \frac{a - (b - c)C\varphi_2}{2cS\varphi_2}, \tag{B4b}$$

According to Eq. (B3b), φ_1 can be expressed by φ_3 and φ_2,

$$\tan(\varphi_1/2) = \frac{2C\varphi_2 S\varphi_3 + S\varphi_2 C\varphi_3 - 3S\varphi_2}{-\sqrt{3}C\varphi_3 - \sqrt{3}}. \tag{B4c}$$

According to Eq. (B3d), φ_4 can be expressed by φ_3 and φ_2,

$$\tan(\varphi_4/2) = \frac{4S\varphi_2 C\varphi_3 + 2C\varphi_2 S\varphi_3}{-2\sqrt{3}S\varphi_2 S\varphi_3 + \sqrt{3}C\varphi_2 C\varphi_3 + \sqrt{3}C\varphi_2}. \tag{B4d}$$

Solving Eqs. (B4b) and (B4c), the dihedral angle φ_3 is eliminated, resulting in the relationship between φ_1 and φ_2 as

$$b^2C^2\varphi_2 - 4cbC\varphi_2 - 2\sqrt{3}c^2S\varphi_2\tan(\varphi_1/2) - 3c^2C^2\varphi_2 + 6c^2 = 0. \tag{B4e}$$

If $c \neq 0$, and $\mu = b/c$ is defined, Eqs. (B4b) and (B4e) becomes,

$$\tan(\varphi_3/2) = \frac{2 - (\mu - 1)C\varphi_2}{2S\varphi_2}, \tag{B5a}$$

and

$$\mu^2C^2\varphi_2 - 4\mu C\varphi_2 - 2\sqrt{3}S\varphi_2\tan(\varphi_1/2) - 3C^2\varphi_2 + 6 = 0, \tag{B5b}$$

respectively. To solve φ_2 from φ_1, Eq. (B5b) can be transformed as

$$T_1\tan^4(\varphi_2/2) + T_2\tan^3(\varphi_2/2) + T_3\tan^2(\varphi_2/2) + T_4\tan(\varphi_2/2) + T_5 = 0, \tag{B5c}$$

in which

$$T_1 = \mu^2 + 4\mu + 3,$$

$$T_2 = -4\sqrt{3}\tan(\varphi_1/2),$$

$$T_3 = 18 - 2\mu^2,$$

$$T_4 = -4\sqrt{3}\tan(\varphi_1/2),$$

$$T_5 = \mu^2 - 4\mu + 3.$$

APPENDIX C. The truss-transformation method

Mobility calculation is rather complicated for spatial linkages especially for multi-loop linkages constructed with overconstrained units. The truss-transformation method [23] is a convenient way. In this method, the target linkage is converted as a mobile truss at first, and then its kinematic indeterminacy can be determined by analysing the equilibrium matrix of the truss [24]. During the conversion process, rigid links connecting two revolute joints are converted to a tetrahedron, triangle or two-tetrahedron assembly depending on the relationship between the corresponding revolute axes, each revolute joint is converted to a line along the revolute axis with a pair of spherical joints, and aunit length is generally chosen as the distance between these spherical joints.

For a truss with j joints and b bars, its equilibrium equation can be established as follow

$$\mathbf{H}\cdot\mathbf{t}=\mathbf{f}. \tag{C1}$$

where $\mathbf{H}$ is the equilibrium matrix with dimensions $3j$ by b, $\mathbf{t}$ is the vector of bar forces with dimensions b by one, and $\mathbf{f}$ is the vector for load on joints with dimensions $3j$ by one. Here, we only consider the truss without external forces, i.e., $\mathbf{f}=\mathbf{0}$. Then

$$\mathbf{H}\cdot\mathbf{t}=\mathbf{0}. \tag{C2}$$

Take r as the rank of $\mathbf{H}$, the system will generate some self-stress with the number

$$s=b-r. \tag{C3}$$

According to structural mechanics, the following compatibility equations should be satisfied

$$\mathbf{C}\cdot\mathbf{d}=\mathbf{e}, \tag{C4}$$

where $\mathbf{d}$ is the vector of node displacements, $\mathbf{e}$ is for the bar elongations, $\mathbf{C}$ is the compatibility matrix. Since links are always assumed to be rigid in the mechanism theory, there is no elongation of bars here, i.e., $\mathbf{e}=\mathbf{0}$. Therefore, the compatity equations become homogeneous ones

$$\mathbf{C}\cdot\mathbf{d}=\mathbf{0}. \tag{C5}$$

According to the virtual work, the compatibility matrix is the transposition of the equilibrium matrix

$$\mathbf{C}=\mathbf{H}^{\mathrm{T}}. \tag{C6}$$

Therefore, the number of inextensional mechanisms (mobility) [24] is

$$m=3j-r-6, \tag{C7}$$

where 6 is for the rigid body motion of the entire truss.

Hereto, the mobility, m, and the overconstraint of the 3D linkages, s, can be obtained by the truss-transformation method at the same time.

Then, filtering ground bars, for equilibrium matrix $\mathbf{H}'$ with dimensions $3j'$ by b and rank r, there exist a $3j'$ by $3j'$ orthogonal matrix $\mathbf{U}=[\mathbf{u}_1, \ldots, \mathbf{u}_{3j'}]$, a b' by b' orthogonal matrix $\mathbf{W}=[\mathbf{w}_1, \ldots, \mathbf{w}_{b'}]$, and a $3j'$ by b' matrix $\mathbf{V}$ with r positive elements $v_i(i=1, \ldots, r)$ on the leading diagonal, such that the SVD of the equilibrium matrix $\mathbf{H}'$ is

$$\mathbf{H}'=\mathbf{UVW}^T \tag{C8}$$

According to Eq. (C7), the set of left singular vectors $\mathbf{U}$, the set of right singular vectors $\mathbf{W}$, and the set of non-zero singular values $\mathbf{V}$ are

$$\mathbf{U}=[\mathbf{u}_1,\cdots,\mathbf{u}_r,\mathbf{u}_{r+1},\cdots,\mathbf{u}_{r+m}], \tag{C9}$$

$$\mathbf{W}=[\mathbf{w}_1,\cdots,\mathbf{w}_r,\mathbf{w}_{r+1},\cdots,\mathbf{w}_{r+s}], \tag{C10}$$

$$\mathbf{V}=\begin{bmatrix} diag(\mathrm{v}_1,\cdots,\mathrm{v}_r) & \mathbf{0} \\ \mathbf{0} & \mathbf{0} \end{bmatrix}. \tag{C11}$$

As each linkage obtained by our method is always with one DOF, $\mathbf{U}$ becomes

$$\mathbf{U}=[\mathbf{u}_1,\cdots,\mathbf{u}_r,\mathbf{u}_{r+1}], \tag{C12}$$

and it moves along a determined kinematic path, and the left nullspace of $\mathbf{H}'$, $\mathbf{u}_{r+1}$, is the precisely space according to [24]. If the current configuration of the mobile truss is denoted as $\mathbf{R}^i$, then the next configuration is predicted as

$$\mathbf{R}^{i'}=\mathbf{R}^i+\mathbf{u}^i_{r+1}\eta, \tag{C13}$$

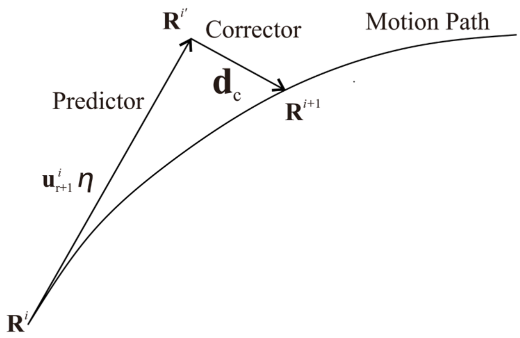

Fig. C1. Predictor-corrector algorithm in each iteration step of the numerical method proposed by Kumar and Pellegrino [26]

η is used to control the transformation speed. As the configuration $\mathbf{R}^{i'}$ is not an exact one in the motion path, the bars of the truss will undergo extensions $\mathbf{e}$. A set of correcting displacement $\mathbf{d}_c$ on all vertices is adopted to eliminate those extensions to correct the configuration [26],

$$\mathbf{d}_c = -\sum_{i=1}^{r} \frac{\mathbf{w}_i^{\mathrm{T}}\mathbf{e}}{v_i}\mathbf{u}_i. \tag{C14}$$

Therefore, $\mathbf{R}^{i+1} = \mathbf{R}^{i'} + \mathbf{d}_c$ is the strain-free configuration nearest to $\mathbf{R}^{i}$, and Fig. C1 shows operations of one step in the iteration process. This corrector step may be repeated a number of times until a desired convergence accuracy is achieved.

Meanwhile, since the rank of **H**' is related to the number of non-zero singular values in **V**, instantaneous mobility thus equals the number of zero-valued singular values in **V**. Therefore, bifurcation positions can be detected by singular values of **V** during the moving process.

References

[1] A. Mazzucchi, A kinetic module for modular structures based on rigid origami, Nexus Network Journal 20 (2017) 1–17.
[2] Resch, R.D., 1968, "Self-supporting structural unit having a series of repetitious geometrical modules," U.S. Patent 3407558.
[3] R.D. Resch, The topological design of sculptural and architectural systems, in: Proceedings of the June 4-8, 1973, national computer conference and exposition, ACM, New York, 1973, pp. 643–650. June 4-8.
[4] T. Tachi, Designing freeform origami tessellations by generalizing Resch's patterns, J Mech Design 135 (2013), 111006.
[5] C.C. Chu, C.K. Keong, The review on tessellation origami inspired folded structure, AIP Conference Proceedings 1892 (2017), 020025.
[6] E. Davis, E.D. Demaine, M.L. Demaine, J. Ramseyer, Reconstructing David Huffman's origami tessellations, J Mech Design 135 (2013), 111010.
[7] Y. Li, Motion paths finding for multi-degree-of-freedom mechanisms, International Journal of Mechanical Sciences 185 (2020), 105709.
[8] M.A.E. Kshad, C. Popinigis, H.E. Naguib, 3D printing of Ron-Resch-like origami cores for compression and impact load damping, Smart Mater. Struct. 28 (2019), 015027 (15pp).
[9] C. Lv, D. Krishnaraju, G. Konjevod, H. Yu, H. Jiang, Origami based mechanical metamaterials, Sci. Rep. 4 (2014) 5979.
[10] L. Magliozzi, A. Micheletti, A. Pizzigoni, G. Ruscica, On the design of origami structures with a continuum of equilibrium shapes, Composites Part B: Engineering 115 (2017) 144–150.
[11] Z. Chen, T. Wu, G. Nian, Y. Shan, X. Liang, H. Jiang, S. Qu, Ron Resch origami pattern inspired energy absorption structures, Journal of Applied Mechanics 86 (2018), 011005.
[12] M. Pesenti, G. Masera, F. Fiorito, Shaping an origami shading device through visual and thermal simulations, Energy Procedia 78 (2015) 346–351.
[13] A. Deng, B. Ji, X. Zhou, Z. You, Geometric design and mechanical properties of foldcores based on the generalized Resch patterns, Thin-Walled Structures 148 (2020), 106516.
[14] Yu, Y., Chen, Y. & Paulino, G.H., 2020, "On the unfolding process of triangular Resch patterns: a finite particle method investigation," In Proceedings of the ASME 2019 International Design Engineering Technical Conferences, Anaheim, CA, USA, August 18-21, 2019, V05BT07A048.
[15] X. Zhang, Y. Chen, Vertex-splitting on a diamond origami pattern, Journal of Mechanisms and Robotics 11 (2019), 031014.
[16] Hull, T. & Tachi, T., 2017, "Double-line rigid origami," In Proceedings ofthe 11th Asian Forum on Graphic Science (AFGS 2017), Tokyo, Aug. 6-10.
[17] Y. Chen, R. Peng, Z. You, Origami of thick panels, Science 349 (2015) 396–400.
[18] Y. Li, Motion paths finding for multi-degree-of-freedom mechanisms, IJMS 185 (2020), 105709.
[19] Y. Chen, Z. You, T. Tarnai, Threefold-symmetric Bricard linkages for deployable structures, Int. J. Solids Struct. 42 (2005) 2287–2301.
[20] J. Denavit, R.S. Hartenberg, A kinematic notation for lower-pair mechanisms based on matrices, Journal of Applied Mechanics 22 (1955) 215–221.
[21] H. Feng, Y. Chen, J.S. Dai, G. Gogu, Kinematic study of the general plane-symmetric Bricard linkage and its bifurcation variations, Mech Mach Theory 116 (2017) 89–104.
[22] T.G. Ionescu, Terminology for mechanisms and machine science, Mech Mach Theory 38 (7-10) (2003) 597–1112.
[23] F. Yang, Y. Chen, R. Kang, J. Ma, Truss transformation method to obtain the non-overconstrained forms of 3D overconstrained linkages, Mech Mach Theory 102 (2016) 149–166.
[24] S. Pellegrino, C.R. Calladine, Matrix analysis of statically and kinematically indeterminate frameworks, Int. J. Solids Struct. 22 (4) (1986) 409–428.
[25] L.H. Dudte, E. Vouga, T. Tachi, L. Mahadevan, Programming curvature using origami tessellations, Nat. Mater. 15 (2016) 583–588.
[26] P. Kumar, S. Pellegrino, Computation of kinematic paths and bifurcation points, Int. J. Solids Struct. 37 (46-47) (2000) 7003–7027.